

Revisiting the Frictional Control of the Antarctic Circumpolar Current From the Energy Diagram

Takuro Matsuta^a, Yuki Tanaka^b and Atsushi Kubokawa^a

^a Faculty of Environmental Earth Science, Hokkaido University, *Sapporo, Japan*

^b Department of Ocean Sciences, Tokyo University of Marine Science and Technology, *Minato-ku, Japan*

Corresponding author: Takuro Matsuta, matsuta@ees.hokudai.ac.jp

ABSTRACT

The transport of the Antarctic Circumpolar Current (ACC) has been shown to increase with friction. Previous studies explained this counter-intuitive relationship called *frictional control* based on the eddy geometric parametrizations. They focused on the eddy momentum transfer and eddy energetics. To maintain the balance between wind stress and eddy interfacial form stress, eddy energy must remain unchanged as friction increases; this requires enhanced baroclinicity to compensate for stronger eddy energy dissipation. However, the independence of eddy energy has not been fully verified, and this interpretation assumes negligible barotropic energy conversion. To address these gaps, we conduct sensitivity experiments in an idealized stratified reentrant channel with varying bottom drag. Numerical simulations show that eddy energy changes substantially with friction. Furthermore, in the high-drag regime, baroclinic energy conversion dominates eddy energy generation, whereas in the low-drag regime barotropic energy conversion contributes substantially. Despite these differences, baroclinicity increases with eddy energy dissipation across all regimes, although the relationship is weak in the low-drag regime owing to barotropic energy conversion. To explain this phenomenon, we extend the frictional control framework independent of any specific eddy parameterization. A simple scaling argument leads to a generalized frictional control, $s \sim D(E)/\tau_w$, where s is baroclinicity, $D(E)$ is eddy energy dissipation, and τ_w is wind stress. This framework provides a natural extension of the existing framework and successfully explains the numerical results. These results indicate that eddy dissipation controls the baroclinicity; therefore, properly parameterizing the eddy dissipation rate is essential for representing ACC dynamics in ocean models.

1. Introduction

Ocean circulation is driven by external forcing, including wind stress, heat flux, and tidal mixing. Energy budget studies suggest that the adiabatic component of ocean circulation is sustained by wind stress (Von Storch et al. 2012; Zemskova et al. 2015). Wind stress drives upwelling and enhances the isopycnal slope, which tends to increase available potential energy (APE) (Roquet et al. 2011; Aiki et al. 2011). The APE gained is released by baroclinic energy conversion. The Antarctic Circumpolar Current (ACC) is one of the hotspots of baroclinic energy conversion since there exist strong westerlies in the Southern Ocean. Because of this importance, the ACC energy cycle has been the subject of extensive research.

Eddy energy in the ACC has been discussed in the framework of the Lorenz energy cycle (LEC) (e.g., Aiki and Richards 2008; Von Storch et al. 2012; Chen et al. 2014; Zemskova et al. 2015; Wu et al. 2017; Matsuta and Masumoto 2023; Matsuta et al. 2024). The LEC quantifies energy conversions among mean kinetic energy (MKE), mean available potential energy (MAPE), eddy available potential energy (EAPE), and eddy kinetic energy (EKE). These studies showed that much of the energy input to the ACC is dissipated in the surface layer, which sustains the Ekman spiral (Roquet et al. 2011; Matsuta and Masumoto 2023), while the remainder is transferred to eddy kinetic energy (EKE) through baroclinic energy pathway. Recent research has suggested that baroclinic energy conversion in the ACC is localized downstream of significant topographies (Youngs et al. 2017; Wu et al. 2017; Matsuta and Masumoto 2023; Matsuta et al. 2024), because standing meanders enhance the baroclinic growth rate downstream of topography while suppressing isopycnal steepening far from topography (Thompson and Naveira Garabato 2014; Abernathy and Cessi 2014; Bischoff and Thompson 2014). Matsuta and Masumoto (2023) estimated that more than 70% of baroclinic energy conversion in the ACC is localized downstream of five major topographic obstacles. These studies indicate that flow-topographic interactions control the ACC energy balance. It should be also noted that although previous studies have shown that baroclinic energy conversion dominates EKE generation, the contribution of barotropic energy conversion differs among studies. Some suggest that, when integrated over the entire ACC, its contribution is negligible (Chen et al. 2014; Matsuta and Masumoto 2023; Matsuta et al. 2024), whereas others argue that under strengthened westerly winds it can make a non-negligible contribution (Youngs et al. 2017; Wu et al. 2017).

Recent studies have pointed out that baroclinic energy conversion plays an important role in determining the sensitivity of baroclinicity to friction (Hogg and Blundell 2006; Nadeau and Straub 2012; Nadeau and Ferrari 2015; Marshall et al. 2017; Mak et al. 2017; Yang et al. 2018; Jouanno and Capet 2020; Klymak et al. 2021; Stewart et al. 2023; Yang et al. 2023; Maddison et al. 2025). Here, *baroclinicity* refers to the meridional slope of the isopycnal surface. These studies showed that as friction increases, baroclinicity and hence circumpolar transport increases. Marshall et al. (2017) explained this counter-intuitive relationship focusing on the eddy momentum transfer and eddy energetics. If transient eddies are responsible for the equilibrium of the ACC, transient eddies should transport surface stress downward to ultimately be removed at the bottom (Johnson and Bryden 1989). They assumed that the eddy interfacial form stress is scaled by eddy energy as αE based on the eddy geometric parametrization (Marshall et al. 2012), where E is the eddy energy and α is a tuning parameter associated with the eddy geometric parameterization. Since the eddy interfacial form stress should balance the wind momentum input if the residual circulation vanishes (Marshall and Radko 2003), the eddy energy is scaled by the wind stress,

$$\alpha E \sim \tau_0, \quad (1)$$

where τ_0 is the wind stress strength. If α can be regarded as a constant, this scaling indicates that eddy energy is constrained by wind stress and not dependent on friction. In order to maintain this momentum balance, the baroclinic energy conversion should sustain the eddy energy against the dissipation λE , where λ is eddy dissipation rate. Since the baroclinic energy conversion is dependent on the baroclinicity and eddy interfacial form stress, the increase in the friction (Marshall et al. 2017; Mak et al. 2017; Klymak et al. 2021) or eddy energy dissipation rate (Mak et al. 2022a,b; Yang et al. 2023) requires an increase in the baroclinicity,

$$\alpha E s \sim \lambda E,$$

or

$$s \sim \frac{\lambda}{\alpha}, \quad (2)$$

where s is the baroclinicity. Marshall et al. (2017) referred to this mechanism as *frictional control*.

A key feature missing in the frictional control mechanism is flow-topographic interactions. According to Rivière et al. (2004), when the bottom drag coefficient is low, the barotropic

mode dominates the mean flow, causing the mean flow to be more strongly influenced by bottom topography. In addition, Stewart et al. (2023) also noted that friction may modify impacts of standing meanders. This may result in the increase in the barotropic energy conversion due to an enhanced standing meander downstream of the ridge (Youngs et al. 2017), even though the frictional control mechanism implicitly assumes that EKE is generated only through baroclinic instability. However, previous studies discussing the frictional control mechanism did not explicitly estimate barotropic and baroclinic energy conversion rates, nor did they confirm the validity of this assumption.

It is also necessary to revisit the drag dependence of eddy energy. In the framework of frictional control, (1) predicts that eddy energy is independent of friction. However, Figure 2 in Marshall et al. (2017) suggests that EKE decreases as the drag coefficient increases in the regime below $r = 10^{-3} \text{ m s}^{-1}$, while EKE is less sensitive in the high-drag regime of $r \geq 10^{-3} \text{ m s}^{-1}$.

To address these gaps, we conduct a series of sensitivity experiments by changing the drag coefficient. We evaluate the drag dependence of eddy energy and standing meanders in each regime. We also examine how barotropic and baroclinic energy conversions change across different drag regimes using the LEC. By combining these analyses, we propose a generalized frictional control relation that extends the formulation of previous studies.

This study is organized as follows. Section 2 describes the model configurations. In Section 3, we investigate the dependency of eddy energy and LEC on the drag coefficient through numerical experiments. Section 4 proposes a generalized frictional control. Section 5 provides a summary of this study.

2. Methods

2.1 Model configuration

We use MITgcm (Marshall et al. 1997) in the Boussinesq and hydrostatic approximations on the β plane. The domain is 4000-km long (zonal, x -direction), 2000-km wide (meridional, y -direction), and 3881-m deep (vertical, z -direction). A free-slip boundary condition is imposed at the northern and southern boundaries and a periodic boundary condition is in the zonal direction. There is no heat transport across the southern boundary. We used a Cartesian grid with a horizontal resolution of 10×10 km. There are 29 vertical levels increasing in thickness from 8.5 m at the ocean surface to 248 m at depth. The Coriolis parameter is $f = f_0 + \beta y$, with $f_0 = -10^{-4} \text{ s}^{-1}$ and $\beta = 10^{-11} \text{ m}^{-1} \text{ s}^{-1}$. We used a reference density ρ_0 of 1035 kg m^{-3} . The density is prescribed by a temperature-only linear equation of state with a thermal expansion coefficient of $2.0 \times 10^{-4} \text{ }^\circ\text{C}^{-1}$. The subgrid horizontal and vertical eddy viscosity are $100 \text{ m}^2 \text{ s}^{-1}$ and $3.0 \times 10^{-4} \text{ m}^2 \text{ s}^{-1}$, respectively, while the subgrid horizontal and vertical eddy diffusivities are zero and $5.0 \times 10^{-6} \text{ m}^2 \text{ s}^{-1}$. To represent a surface mixed layer, we employed the K-profile parameterization (KPP) mixing scheme (Large et al. 1994). The bottom topography consists of a Gaussian ridge centered at $x_0 = 1000$ km:

$$\eta_b(x, y) = h_0 \exp\left[-\frac{(x - x_0)^2}{\sigma_x^2}\right], \quad (3)$$

where $h_0 = 1500$ m and $\sigma_x = 300$ km. Hence, the ocean thickness is given as $h = H_0 - \eta_b$, where $H_0 = 3881$ m. The wind stress is expressed as:

$$\tau_w(y) = \tau_0 \sin\left(\pi \frac{y}{L_y}\right), \quad 0 \leq y \leq L_y, \quad (4)$$

where $\tau_0 = 0.2 \text{ N m}^{-2}$ and $L_y = 2000$ km is the meridional extent of the domain. At the northern boundary, the temperature is relaxed to an exponential profile ranging from 8°C at the surface to 0°C at the bottom:

$$\theta(z) = \frac{8 \left(e^{\frac{z}{h_{sc}}} - e^{-\frac{H_0}{h_{sc}}} \right)}{\left(1 - e^{-\frac{H_0}{h_{sc}}} \right)}, \quad (5)$$

where θ is the potential temperature and $h_{sc} = 1000$ m is the scale height. The initial stratification is also based on this profile.

The bottom drag is represented using a linear function of the bottom velocity. A central aim of this work is to investigate how eddy energetics depend on the bottom linear drag coefficient:

$$r = \{10^{-2}, 7.5 \times 10^{-3}, 5.0 \times 10^{-3}, 2.5 \times 10^{-3}, 10^{-3}, 7.5 \times 10^{-4}, 5.0 \times 10^{-4}, 2.5 \times 10^{-4}, 10^{-4}, 7.5 \times 10^{-5}, 5.0 \times 10^{-5}, 10^{-5}, 10^{-7}\}[\text{m s}^{-1}].$$

Although dissipation processes depend on more complex processes (e.g. lee waves, inverse cascade, spontaneous emission), there are some suggestions that non-propagating form drag by rough topography can be scaled by a linear drag (Klymak 2018; Klymak et al. 2021). Therefore, changing the linear drag coefficient might be regarded as an approximation to changing the effective height of mesoscale topography.

Because a stratified channel model reaches mechanical equilibrium within approximately 40 years (Ward and Hogg 2011), all cases are integrated for 50 years, with the final five years utilized for calculations. For representative cases, simulations are integrated for 100 years, and are confirmed that our results are not dependent on the averaged periods. It should be noted that reaching a thermal equilibrium state would require integrations of roughly 1000 years (Munday et al. 2015), but this is not computationally feasible.

2.2 Energy conversion between eddy and mean flow

We calculate the energy cycle of reentrant channels by considering Lorenz energy cycle (LEC) (Lorenz 1955) linking mean kinetic energy (MKE), K_M , eddy kinetic energy (EKE), K_E , mean available potential energy (MAPE), P_M , and eddy available potential energy (EAPE), P_E (Figure 1). The derivation of this diagram follows standard textbooks (e.g., Olbers et al. 2012).

At any given location $\mathbf{x} = (x, y, z)$ we define:

$$K_M(x, y, z) = \frac{1}{2} \rho_0 (\overline{u^2} + \overline{v^2}), \quad (6)$$

$$K_E(x, y, z) = \frac{1}{2} \rho_0 (\overline{u'^2} + \overline{v'^2}), \quad (7)$$

$$P_M(x, y, z) = -\frac{1}{2} \frac{g}{\partial_z \rho_{bg}(z)} \overline{\rho^{*2}}, \quad (8)$$

and

$$P_E(x, y, z) = -\frac{1}{2} \frac{g}{\partial_z \rho_{bg}(z)} \overline{\rho'^2}, \quad (9)$$

where $\mathbf{u} = (u, v, w)$ is the velocity field, $g = 9.81 \text{ m s}^{-2}$ is the gravitational acceleration, the overbar denotes a time average (in our simulations, taken over the final 5-year period), and the prime denotes a transient eddy component defined as the deviation from the time average. References to *eddy* denote a transient eddy hereafter. The background density ρ_{bg} is defined as horizontally averaged mean density. The deviation of density from the background state is defined as

$$\rho^*(t, x, y, z) = \rho(t, x, y, z) - \rho_{bg}(z). \quad (10)$$

With this definition,

$$\rho' = \rho - \bar{\rho} = (\rho^* + \rho_{bg}) - \overline{\rho^* + \rho_{bg}} = \rho^* - \overline{\rho^*}. \quad (11)$$

In our simulations, the energy input is described as:

$$I_W = \iint \boldsymbol{\tau}_w \cdot \overline{\mathbf{u}}_h^{(0)} dx dy, \quad (12)$$

where $\boldsymbol{\tau}_w$ is the surface wind stress and $\mathbf{u}_h^{(0)}$ is the surface horizontal flow. The integration is performed over the channel. Note that although the westerly wind forcing is identical across the numerical experiments, the energy input differs depending on the friction. The objective of this study is not to examine how the relative proportions of energy conversion pathways change under a fixed energy input; rather, it is to investigate how the entire energy diagram—including the energy input itself—changes when the same westerly wind forcing is applied.

The energy supplied by the wind is redistributed among the four energy reservoirs through energy conversion terms, as shown in Figure 1. The conversion between MKE and MAPE is:

$$\begin{aligned} C(K_M, P_M) &= \iiint g \overline{\rho^*} \overline{w} \, dx dy dz = \iiint \overline{\mathbf{u}_h} \cdot \overline{\nabla_h p} \, dx dy dz \\ &= \iiint \overline{\mathbf{u}_{h,a}} \cdot \overline{\nabla_h p} \, dx dy dz, \end{aligned} \quad (13)$$

where p is pressure, $\mathbf{u}_h = (u, v)$ is the horizontal velocity field, $\mathbf{u}_{h,a}$ is the ageostrophic component, and ∇_h is the horizontal gradient operator. A positive sign for $C(K_M, P_M)$ indicates energy draining to MAPE from MKE.

The conversion from MAPE to EAPE is

$$C(P_M, P_E) = \iiint \frac{g}{\partial_z \rho_{bg}(z)} \overline{\rho' \mathbf{u}'_h} \cdot \nabla_h \overline{\rho^*} \, dx dy dz, \quad (14)$$

which is the baroclinic conversion rate (BCR), indicating, when positive, that eddies are extracting potential energy from the mean stratification. Because a mixed layer exists in roughly the upper 400 m, the vertical density gradient becomes extremely small there, which leads to unrealistically large values of BCR. To avoid this problem, the background density gradient in the upper 450 m is estimated as the density gradient between the ocean surface and 450 m depth. Similarly, the conversion from EAPE to EKE is:

$$C(P_E, K_E) = - \iiint g \overline{\rho' w'} \, dx dy dz, \quad (15)$$

which is the vertical eddy density flux (VEDF). A positive value of VEDF corresponds to the EKE generation by releasing EAPE. We refer to the energy pathway of $K_M \rightarrow P_M \rightarrow P_E \rightarrow K_E$ as *baroclinic energy pathway*.

The barotropic energy conversion rate (BTR), $C(K_M, K_E)$ is defined as:

$$\begin{aligned}
C(K_M, K_E) &= \rho_0 \iiint (\bar{u} \nabla \cdot \overline{u' \mathbf{u}'} + \bar{v} \nabla \cdot \overline{v' \mathbf{u}'}) dx dy dz \\
&= -\rho_0 \iiint (\overline{u' \mathbf{u}'} \cdot \nabla \bar{u} + \overline{v' \mathbf{u}'} \cdot \nabla \bar{v}) dx dy dz,
\end{aligned} \tag{16}$$

where ∇ is the three-dimensional gradient operator. A positive sign indicates EKE generation by barotropic instability (Pedlosky 1987). We refer to the energy pathway of $K_M \rightarrow K_E$ as *barotropic energy pathway*.

The energy inputted to the system is finally balanced by MKE and EKE dissipation by viscosity and bottom friction, indicated by $D(K_M)$ and $D(K_E)$, respectively. In addition, the northern sponge layer and diffusivity act as both source and sink for the APE, which are merged into $D(P_M)$ and $D(P_E)$ in the energy diagram.

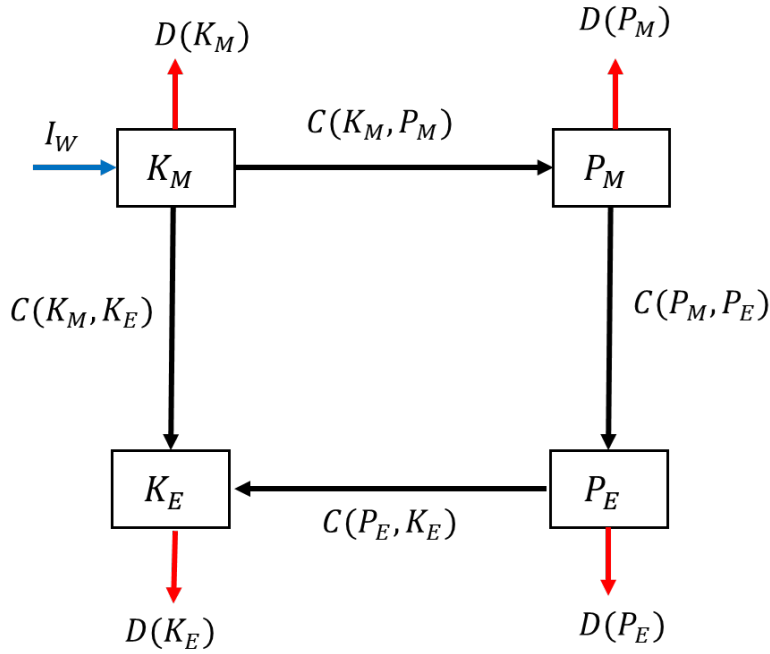


Figure 1. Four-box energy diagram among K_M , K_E , P_M , and P_E . Each reservoir is connected by energy conversion functions indicated by $C(*,*)$. Energy generation and dissipation by subgrid processes in each reservoir is denoted by $D(*)$, indicated by red arrows. In our simulation, the reentrant channels are driven by westerlies (I_W in the diagram, indicated by a blue arrow).

3. Results

3.1 Basic description of mean flow in each drag regime

We first present the dependence of horizontal circulation on the drag coefficient. The barotropic streamfunction is defined as:

$$\psi(x, y) = \int_0^y \int_{-h}^0 \bar{u} \, dz dy. \quad (17)$$

We compare the outputs of $r = 10^{-2} \text{ m s}^{-1}$, (termed “HIGH”), $r = 5 \times 10^{-4} \text{ m s}^{-1}$ (termed “MEDIUM”), and $r = 10^{-5} \text{ m s}^{-1}$ (termed “LOW”) as representative cases of high-drag, medium-drag, and low-drag conditions, respectively. Figure 2 demonstrates that large EKE values are localized in topographic lees, suggesting that eddy activities are constrained by local dynamics as suggested in previous studies (Thompson and Naveira Garabato 2014; Abernathey and Cessi 2014), regardless of the bottom drag coefficient. By contrast, the EKE magnitude appears to depend on friction. We return to this point in the next section.

A key difference in horizontal circulation among the three cases is seen in the strength of wind-driven gyre and standing meander. Figure 2 shows that the curvature of standing meanders increases as drag coefficient reduces. In addition, wind-driven gyre circulations are more evident with decreasing drag. In HIGH, the wind-driven gyre circulations are not evident, suggesting that the ridge does not work as an equivalent western boundary (Wang and Huang 1995; Nadeau and Ferrari 2015): The opposite is true under the low-drag regimes. The differences in sensitivity to bottom topography may be explained by the barotropization of the mean flow. Figure 3 shows the fraction of MKE of the barotropic mode relative to total MKE, integrated over the domain, as a function of drag coefficient. The barotropic mode intensifies as the bottom drag coefficient decreases for $r \geq 10^{-5} \text{ m s}^{-1}$, and the fraction reaches 85 % at $r = 10^{-5} \text{ m s}^{-1}$, indicating that the mean flow is approximately barotropic under low-drag conditions. This occurs because the bottom current experiences minor damping under low drag, and the opposite is true for high drag (Rivière et al. 2004; LaCasce 2017). It should be noted that the barotropic mode becomes insensitive to the drag coefficient for $r \leq 10^{-5} \text{ m s}^{-1}$ because the timescale of spindown, $(r/H_0)^{-1}$, is greater than 12 years. Hence, the bottom friction can be neglected in this regime, and the viscosity is responsible for the dissipation.

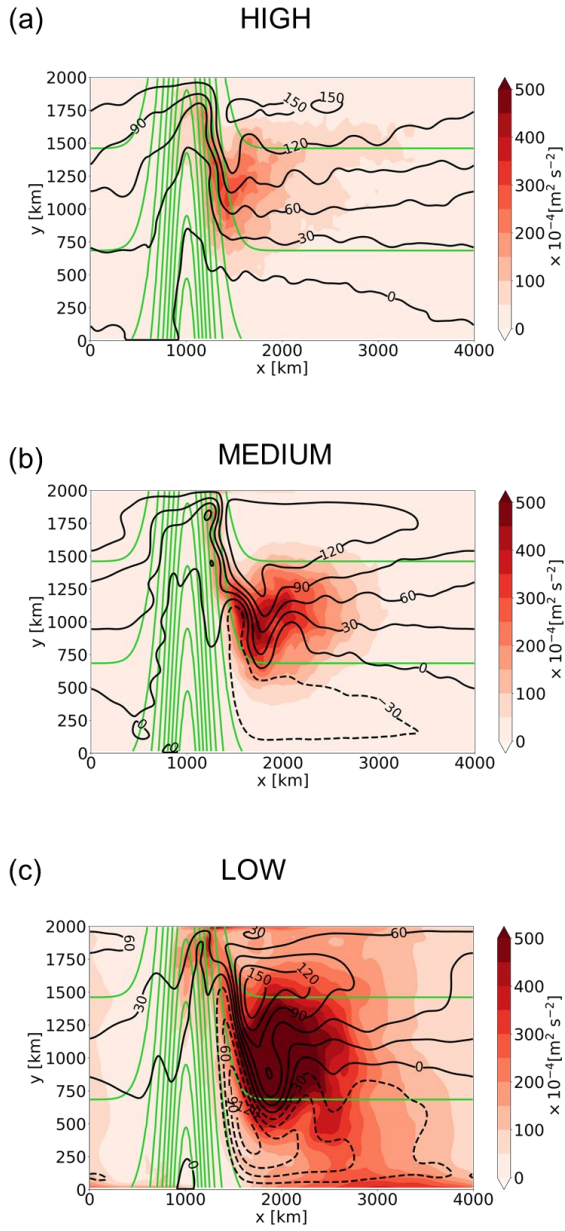


Figure 2. Horizontal distribution of vertically averaged EKE per density (background colors) and barotropic streamfunction contours (black lines, [Sv]) for (a) HIGH, (b) MEDIUM, and (c) LOW. Green lines are geostrophic contours with a contour interval of $2.0 \times 10^{-9} \text{ m}^{-1} \text{ s}^{-1}$. Here, the geostrophic contour is defined as $-(f_0 + \beta y)/h$.

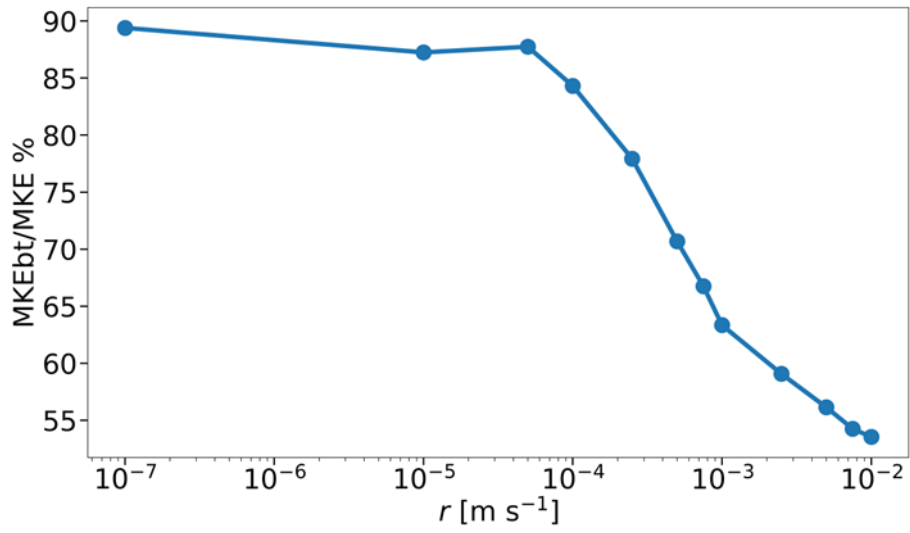


Figure 3. Fraction of the barotropic mode of MKE relative to the total MKE.

3.2 Dependency of eddy energy

Figure 4 provides a quantitative illustration of the dependence of eddy energy on friction. The EKE values reduce with increasing drag coefficient for $r \leq 10^{-3} \text{ m s}^{-1}$, while it is less sensitive in the high-drag regime. This result is consistent with Figure 2 in Marshall et al. (2017). In contrast to EKE, the EAPE values increase with drag coefficient. As a result, the total eddy energy, the sum of EKE and EAPE decreases with the drag coefficient in the regime of $r \leq 10^{-3} \text{ m s}^{-1}$, while it increases in the high-drag regime. These results suggest that eddy energy strongly depends on friction and (1) does not hold in our configuration.

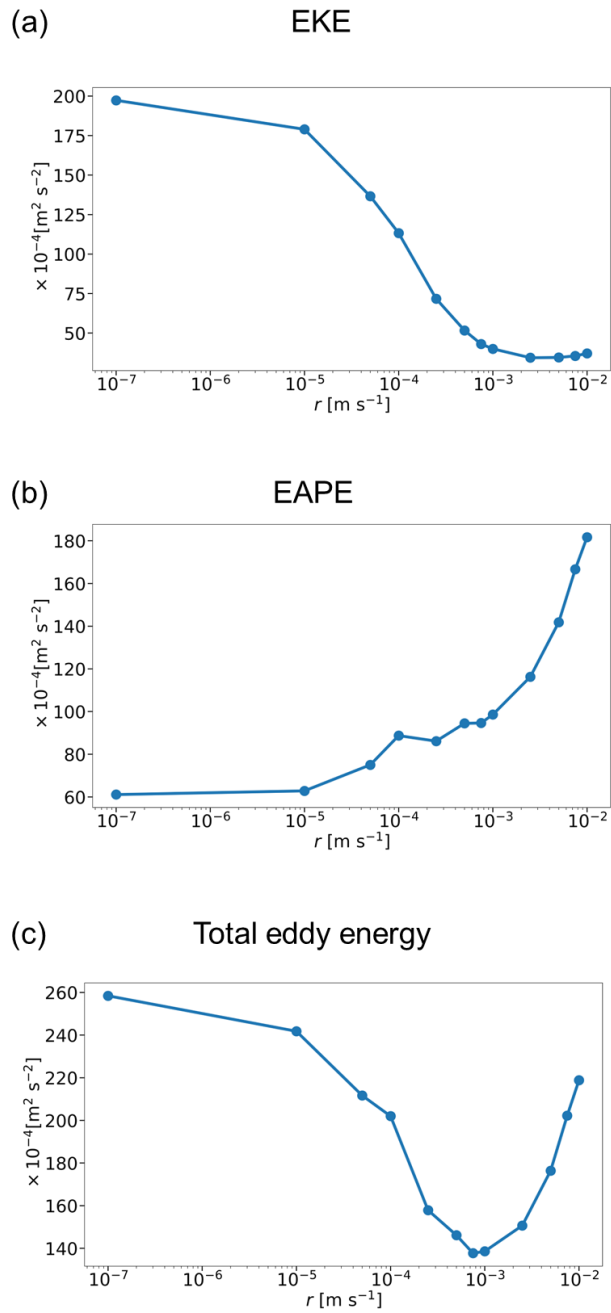


Figure 4 Blue curves indicate domain-averaged (a) EKE, (b) EAPE, and (c) total eddy energy per density as functions of drag coefficients.

3.3 Dependence of BCR and BTR on the linear drag coefficient

We examine the horizontal distribution of VEDF and BTR (Figure 5). We analyze VEDF here rather than BCR because it is unaffected by the rotational component of the eddy flux (Marshall and Shutts 1981) and thus more clearly reflects the net distribution of baroclinic instability. The choice between these two quantities does not change the domain-integrated energy budget analysis and hence the qualitative conclusion. In the HIGH case, VEDF exhibits large positive values downstream of the topography because the standing meander locally intensifies baroclinicity (Thompson and Naveira Garabato 2014; Bischoff and Thompson 2014). For the MEDIUM and LOW cases, the spatial distribution exhibits similar characteristics. However, the amplitude of VEDF decreases with decreasing drag coefficient. In particular, VEDF is confined along the western boundary in the LOW case. The lower panel of Figure 5 demonstrates that the BTR is also localized downstream of topography. In HIGH, the BTR exhibits a patchy structure with both positive and negative values. A similar distribution is found in the ACC of the high-resolution models (Wu et al. 2017; Matsuta and Masumoto 2023). As friction decreases and the standing meander becomes larger, the area of positive BTR widens. Although negative regions still exist in the low-drag regime, as shown below, the BTR becomes positive when integrated over the domain.

To demonstrate the impact of drag coefficient quantitatively, we examine the LEC for HIGH, MEDIUM and LOW. Figure 6 shows that the fate of wind energy varied with the drag coefficient. Under high-drag conditions (Figure 6(a)), nearly 65% of the wind energy is converted to the MAPE. The APE gain is converted into EKE via BCR (86 GW) and VEDF (71 GW). By contrast, the barotropic conversion is negative, implying a transfer of energy from EKE to MKE. This behavior is consistent with the barotropic governor mechanism (James and Gray 1986; Solodoch et al. 2016; Youngs et al. 2017). The barotropic governor refers to the process by which eddies generated through baroclinic conversion produce upgradient momentum fluxes, leading to the extraction of EKE by the horizontal shear of the mean flow. According to Youngs et al. (2017), eddies tilt in the upgradient direction downstream of topography in a stratified reentrant channel model, which is reflected in the negative BTR. Consequently, in the high-drag regime, eddy energy is primarily governed by the baroclinic pathway, with the barotropic pathway providing a weak damping effect.

By contrast, under low-drag conditions (Figure 6(c)), the barotropic route substantially contributes to the EKE generation. Although there are some negative BTR areas, positive BTR is dominant (Figure 5(f)), indicating that enhanced standing meanders facilitate eddy generation via barotropic instability. Negative BTR areas (Figure 5(f)) can arise even if barotropic instability is substantial owing to several processes, including the barotropic governor mechanism, the phase of the standing meander (Takaya and Nakamura 2001; Danielson et al. 2006), and nonlocal eddy–mean flow interactions (Murakami 2011; Chen et al. 2014; Matsuta and Masumoto 2021). Accordingly, we refrain from attributing the negative BTR identified in Figure 5(f) to any single mechanism. In contrast to the enhanced BTR, baroclinic energy pathway is weaker than in the high-drag case: the reduced conversion from MKE to MAPE results in smaller BCR and VEDF. Under medium-drag conditions (Figure 6(b)), the partitioning of energy inputs exhibited characteristics between these two regimes. It should also be noted that the MKE sink shows little change among experiments. Under low-drag conditions, the MKE sink at the ocean floor is naturally reduced; however, this is offset by increased viscous dissipation in the ocean interior due to an enhanced standing meander.

To quantify the dependency of energy conversion rates on the bottom drag, the energy conversion rates are plotted as functions of drag coefficients in Figure 7(a). If the bottom drag is smaller than 10^{-4} m s^{-1} , the contribution of BTR is substantial. The BTR values decrease to zero between $r = 10^{-4} \text{ m s}^{-1}$ and $r = 10^{-3} \text{ m s}^{-1}$ and take small negative values in the high-drag regime. Conversely, $C(K_M, P_M)$, BCR and VEDF increase in tandem with increasing drag coefficient, suggesting that increased bottom drag intensifies the baroclinic energy pathway. The mechanism by which MAPE gain increases with friction is discussed in Appendix. The compensating relationship between barotropic and baroclinic pathways causes the BCR fraction in the eddy energy generation, $\text{BCR}/(\text{BCR} + \text{BTR})$ to vary with the drag coefficient. Figure 7(b) demonstrates that the BCR fraction in the EKE gain is 75 % under the low-drag conditions of $r = 10^{-4} \text{ m s}^{-1}$. It increases sharply to 100 % between $r = 10^{-4} \text{ m s}^{-1}$ and $r = 10^{-3} \text{ m s}^{-1}$.

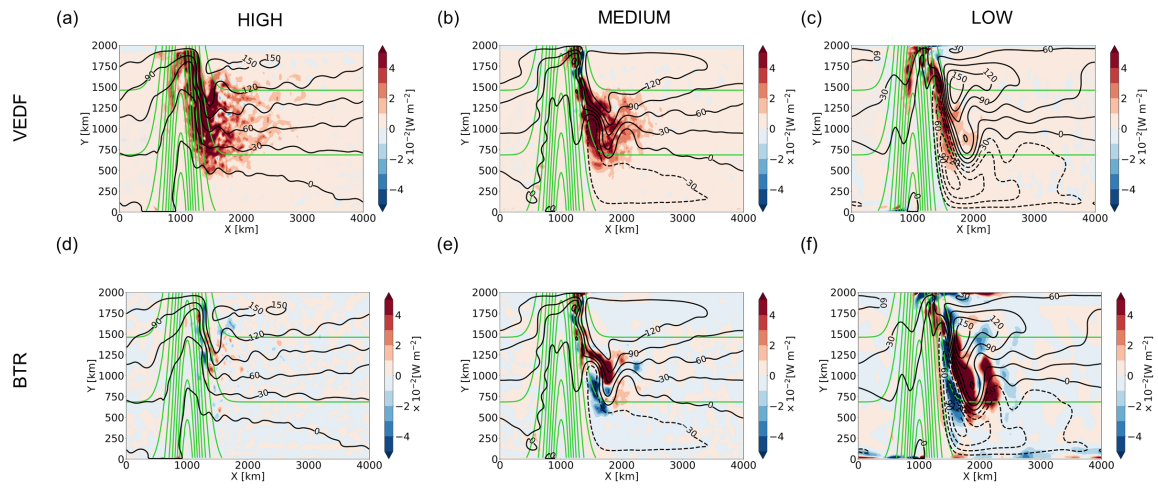


Figure 5 Horizontal distributions of VEDF for (a) HIGH, (b) MEDIUM, and (c) LOW. Green and black contours are the same as those in Figure 2. Lower panels are the same as the upper panel but for BTR.

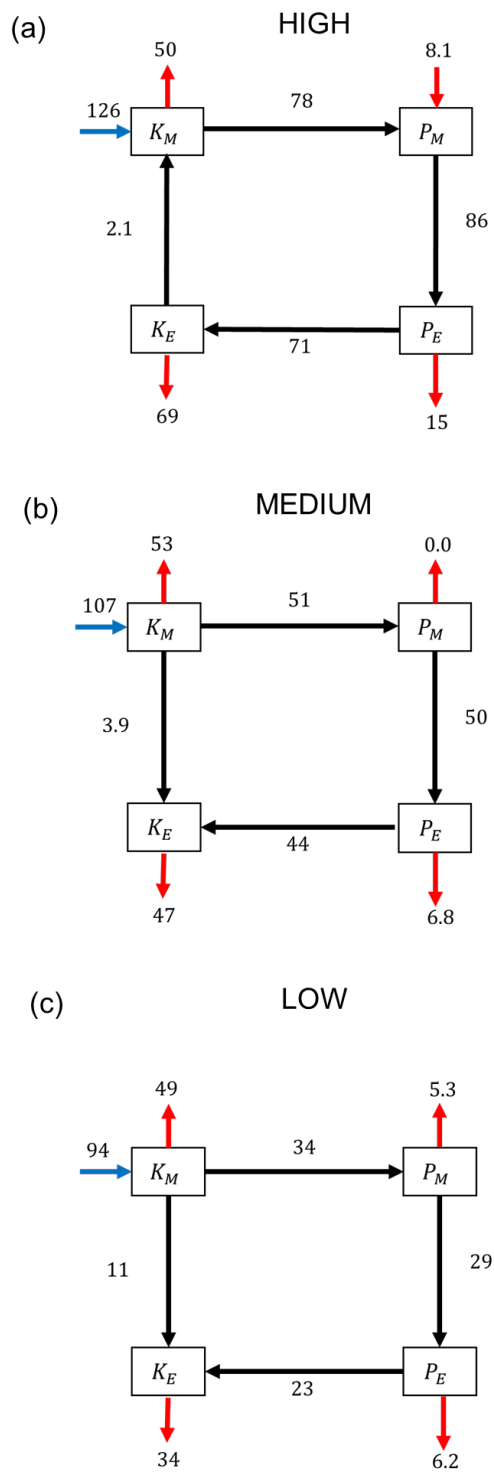
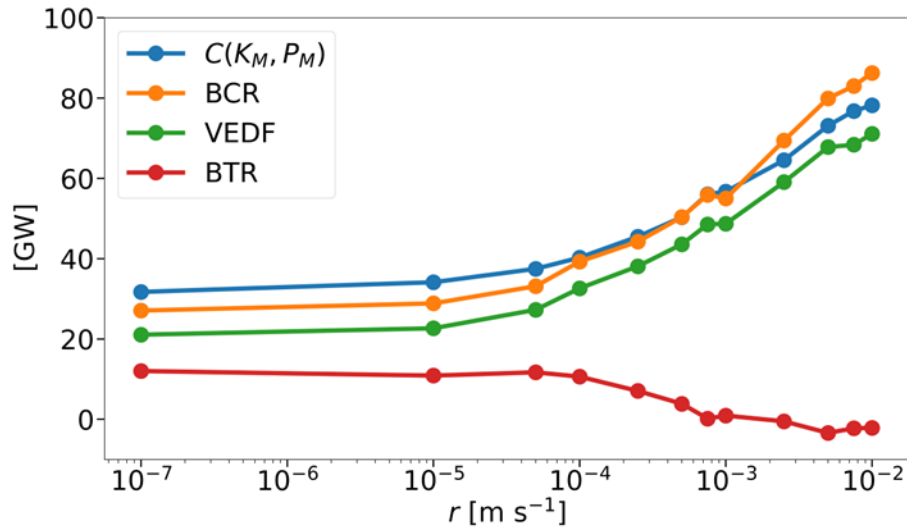


Figure 6. LEC in the same style as Figure 1 calculated for (a) HIGH, (b) MEDIUM, (c) and LOW.

(a) Energy conversion rate



(b) Fraction of baroclinic route

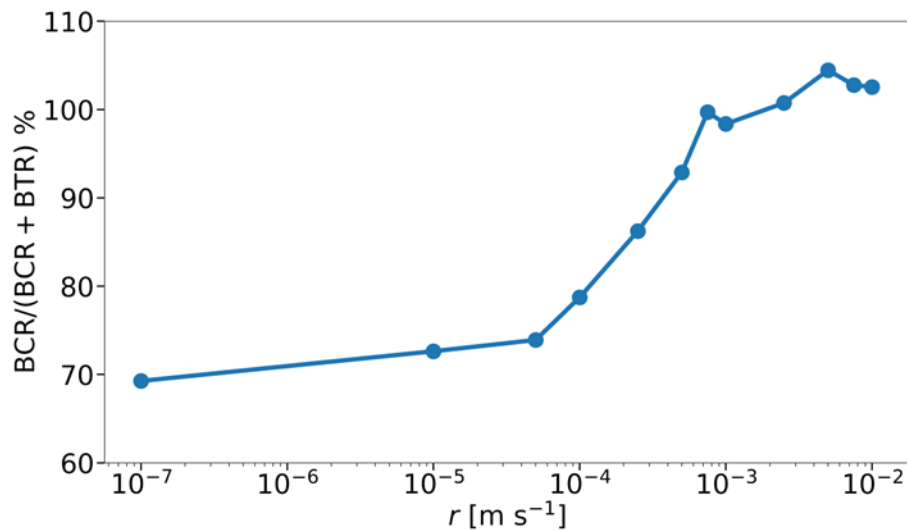


Figure 7. (a) Curves of $C(K_M, P_M)$ (blue line), BCR (orange line), VEDF (green line), and BTR (red line) as functions of drag coefficients. (b) Curves of the fraction of BCR to the sum of BCR and BTR as a function of drag coefficients.

4. Discussion: Generalization of frictional control

Figure 8 illustrates how baroclinicity varies with the drag coefficient. Here, the baroclinicity is defined as the difference in the depth of the 1°C isotherm between $y = 500$ km and $y = 1500$ km in the zonally-averaged mean temperature. The baroclinicity is found to increase with friction even outside the high-drag regime. In the framework of frictional control proposed in previous studies, both (1) and (2) should hold. However, Figure 8 suggests that (2) solely holds even if (1) is not valid (Figure 4).

To reconcile this gap, we generalize the frictional control framework. The key ingredients are the eddy energy balance and eddy interfacial form stress. The eddy energy balance is denoted as

$$\text{BCR} + \text{BTR} = D(K_E) + D(P_E). \quad (18)$$

The first term of the left-hand side is scaled as

$$\text{BCR} \sim \frac{g}{\partial_z \rho_{bg}(z)} \overline{\rho' \mathbf{u}'_h} \cdot \nabla_h \overline{\rho^*} \sim s \tau_w, \quad (19)$$

where s is baroclinicity and τ_w is westerly magnitude. Here, we assumed that eddy interfacial form stress along the density contour is proportional to τ_w ,

$$\frac{\overline{\rho' \mathbf{u}'_h}}{\partial_z \rho_{bg}(z)} \cdot \left(\frac{\nabla_h \overline{\rho^*}}{|\nabla_h \overline{\rho^*}|} \right) \sim \tau_w, \quad (20)$$

because the eddy interfacial form stress transfers the wind momentum towards bottom. This assumption is widely confirmed to be held in stratified channel models (Marshall and Radko 2003; Ward and Hogg 2011; Stewart et al. 2023; Zhang et al. 2024) and in the ACC (Johnson and Bryden 1989; Phillips and Rintoul 2000; Katsumata 2017). The condition of (20) corresponds to (1), but serves different purposes. An advantage of (20) is that it does not rely on any specific eddy parametrization and hence it is suitable for model diagnosis. By contrast, (1) has been introduced to show that an implementation of geometric eddy parameterization (Marshall et al. 2012) can reproduce the frictional control of the ACC in coarse models (Mak et al. 2017, 2018, 2022b). In previous studies, (1) is derived based on the geometric eddy parameterization, assuming that the eddy interfacial form stress scales with eddy energy E and eddy geometric parameter α ,

$$\frac{\overline{\rho' \mathbf{u}'_h}}{\partial_z \rho_{bg}(z)} \cdot \left(\frac{\nabla_h \overline{\rho^*}}{|\nabla_h \overline{\rho^*}|} \right) \sim \alpha E \sim \tau_w. \quad (21)$$

They argued that eddy energy can scale with the wind stress. The disagreement between (1) and numerical results (Figure 4) likely stems from the assumption that the eddy geometric parameter is constant and independent of friction. If BTR is smaller than BCR, (18) and (19) gives

$$s \sim \frac{D(K_E) + D(P_E)}{\tau_w}, \quad (22)$$

which suggests that an increase in eddy energy dissipation leads to an enhancement of baroclinicity under a fixed wind stress. Physically, this implies that, as proposed by Marshall et al. (2017), in order to maintain eddy activities to satisfy (20) against increased eddy energy dissipation, the increased baroclinicity is required to enhance BCR. Therefore, (22) is a generalization of (2).

To validate the scaling of (22), the baroclinicity is compared with $D(K_E) + D(P_E)$ from our experiments. The black dashed curve in Figure 8 shows a function that is proportional to $D(K_E) + D(P_E)$. It captures well the tendency for baroclinicity to increase with increasing friction in all regimes. In particular, in the range of $r \geq 5.0 \times 10^{-4} \text{ m s}^{-1}$, where the BCR is dominant in the eddy energy generation (Figure 7), the changes in eddy energy dissipation and baroclinicity agree very well. In the low-drag regime between $r = 10^{-5} \text{ m s}^{-1}$ and $r = 10^{-4} \text{ m s}^{-1}$, where BTR cannot be neglected, eddy energy dissipation slightly overestimates the change in baroclinicity. Because EAPE depends on the definition of the background state, we verified that similar results are obtained when EKE dissipation is used instead of total eddy energy dissipation (gray dashed curve in Figure 8).

Before closing this section, it is noted that the generalized frictional control (22) includes the implication for *eddy saturation*. Here, eddy saturation indicates the insensitivity of baroclinicity on wind stress. If the eddy-saturated state is achieved, (22) requires that eddy energy dissipation scales with wind stress. In other words, the condition of $D(K_E) + D(P_E) \sim \tau_w$ is a necessary condition of eddy saturation. Physically, this condition implies that eddy saturation is maintained by compensating the excess kinetic energy input associated with strengthened westerly through increase in the eddy energy sink.

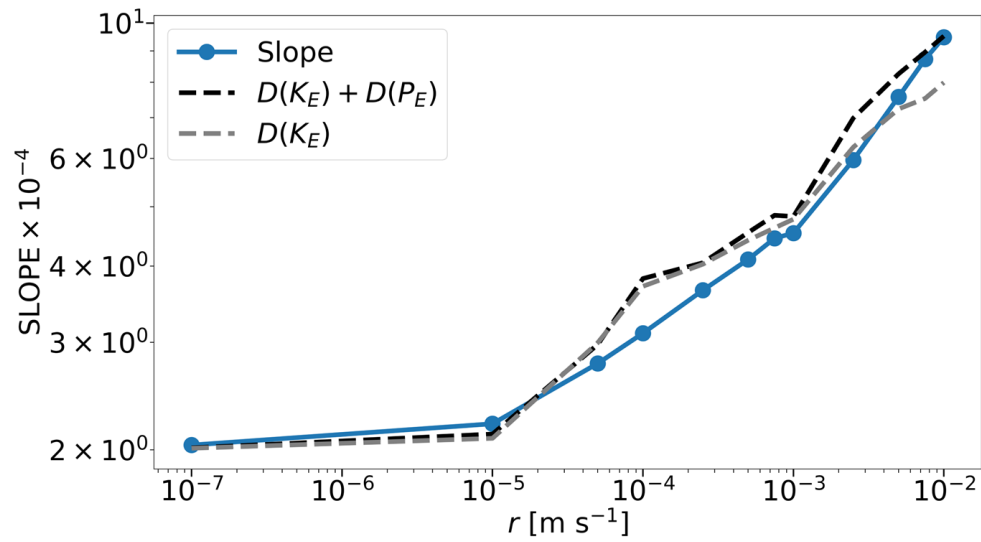


Figure 8 Curve of baroclinicity as a function of drag coefficients. Black and gray dashed curves indicate functions proportional to eddy energy dissipation and EKE dissipation, respectively.

5. Summary and conclusion

In this study, we conducted a series of sensitivity analyses using an idealized reentrant channel model to revisit the frictional control mechanism of the ACC proposed by previous studies. By modifying the drag coefficient, we investigated the dependency of mean flow structures, eddy energy, the LEC, and baroclinicity on friction. Figure 2 shows that the flow becomes more sensitive to bottom topography as the bottom drag coefficient decreases because the mean flow becomes more barotropic (Figure 3). As a result, wind-driven gyre circulations are evident under low-drag conditions, while the zonal circumpolar component is dominant under medium- and high-drag conditions. Although standing meanders are evident in all regimes, those sizes decrease with increasing drag coefficient. We also analyzed the dependency of eddy energy. As shown in Figure 4, EKE is insensitive to bottom drag in the high-drag regime as suggested in previous studies. However, EKE except for the high-drag regime, EAPE, and total eddy energy are strongly dependent on the bottom drag, suggesting that a key ingredient of frictional control (1) is not valid in our configuration. The disagreement between (1) and numerical results suggests that the tuning parameter in the eddy geometric parameterization may need to vary with friction. By analyzing the LEC (Figure 6), it is found that energy pathways depend on the bottom drag coefficient. Under high-drag conditions, a large part of the wind energy is transferred to the APE reservoir, and the APE gain is primarily converted to EKE (Figure 7). By contrast, under low-drag conditions, the barotropic energy pathway became non-negligible owing to enhanced standing meanders (Figure 5). As a result, the BCR fraction in the EKE generation increases with drag coefficients (Figure 7).

Our results suggest that the choice of drag coefficient may be important for realistic ocean general circulation model studies, since the shift in the BCR fraction occurs between 10^{-3} m s^{-1} and 10^{-4} m s^{-1} . In fact, different studies have reported varying contributions of BCR in the ACC. For example, some studies have shown that BCR is dominant in the ACC (Chen et al. 2014; Matsuta and Masumoto 2023; Matsuta et al. 2024), whereas others considered BTR to be non-negligible (Wu et al. 2017). Such inter-model differences in the LECs likely depend on the bottom drag parametrizations.

In section 4, Figure 8 demonstrates that the baroclinicity increases with drag coefficient and (2) is valid under all regimes despite (1) is not valid. To explain this behavior, we

generalized the frictional control framework without relying on any specific eddy parameterization. Instead of assuming that eddy energy can be scaled solely by the wind, i.e., condition (1), we assumed that the eddy interfacial form stress can be scaled by the wind stress. Using this assumption, we scaled the baroclinic conversion term with the wind stress and obtained the generalized frictional control relation. The generalized frictional control (22) suggests that eddy energy dissipation controls baroclinicity, which supports implications of previous studies (Marshall et al. 2017; Mak et al. 2017, 2022a,b; Torres et al. 2025; Eaves et al. 2025). We showed that (22) is in good agreement with the results of our numerical experiments (Figure 8). However, in the low-drag regime, eddy energy dissipation tends to slightly overestimate changes in baroclinicity. Therefore, it should be noted that the accuracy of frictional control decreases as the barotropic energy pathway becomes larger.

We conclude that the frictional control reasonably holds in stratified reentrant channels as long as the baroclinic energy pathway is dominant. Since the baroclinic energy pathway is also dominant in the realistic ACC (e.g., Chen et al. 2014; Matsuta and Masumoto 2023; Matsuta et al. 2024), the eddy energy dissipation is likely to regulate the ACC transport as suggested in previous studies (Mak et al. 2022a,b). To further understand the frictional control mechanism of the real ACC, future work must improve parametrizations of eddy energy dissipation. Although we assumed linear drag for simplicity, the dissipative processes in the real ACC are highly complex, being influenced by tides, topography, and stratification (e.g., Waterman et al. 2013; Naveira Garabato et al. 2013, 2016; Trossman et al. 2016; Yang et al. 2018; Klymak 2018; Hibiya 2021; Takahashi and Hibiya 2021; Klymak et al. 2021; Yang et al. 2023; Zhu et al. 2025). For example, Klymak (2018) and Klymak et al. (2021) suggested that baroclinicity in the ACC increases with increasing mesoscale topographic height. Another study suggested that small-scale topography influences energy transfers and controls the strength of the large-scale jets (Zhu et al. 2025). Furthermore, Yang et al. (2023) suggested that linear drag does not represent the lee wave drag and they suspected that eddy saturation cannot be achieved if the lee wave generation is particularly vigorous. The interplays among eddy, standing meander and dissipative processes should be investigated in future work.

In this study, we have focused on baroclinicity as a mechanism that determines circumpolar transport. However, other mechanisms for frictional control have been proposed in previous studies. Some studies pointed out that the interaction between barotropic instability and standing meanders controls form drag (Constantinou and Young 2017; Constantinou 2018;

Constantinou and Hogg 2019). Matsuta and Mitsudera (2024) also showed that increased nonlinearity of the gyre modifies the form drag, leading to a reduction in transport as friction decreases. Furthermore, we showed that Rossby wave radiation associated with barotropic instability possibly rectifies the barotropic transport (Manuscript to *JPO*), indicating that a parametrization of barotropic eddy flux may be necessary to simulate the barotropic dynamics of ACC (Eaves et al. 2025). Since these previous studies were conducted using unstratified models, future work should examine whether these barotropic mechanisms also operate in stratified models.

Acknowledgments.

Takuro Matsuta was supported by JSPS Grant-in-Aid for JSPS Fellows No. 22J00651 and JSPS Grant-in-Aid No. 24K17120. This work was supported in part by the Collaborative Research Program of Research Institute for Applied Mechanics, Kyushu University, and the Cooperative Research Activities of Collaborative Use of Computing Facility Program (JURCAOSCFG25-06) of Atmosphere and Ocean Research Institute, The University of Tokyo. This research was conducted using the FUJITSU Supercomputer PRIMEHPC FX1000 and FUJITSU Server PRIMERGY GX2570 (Wisteria/BDEC-01) at the Information Technology Center, The University of Tokyo.

Data Availability Statement.

MITgcm is available at <https://mitgcm.readthedocs.io/en/latest/index.html>.

Appendix: Suppression of energy conversion from MKE to MAPE

To investigate the mechanism that suppressed the energy conversion from MKE to MAPE under low-drag conditions, we decompose the MAPE gain into the Ekman transport component and ageostrophic component in the ocean interior. A simple calculation shows that the energy input to the geostrophic component is balanced by the work of the Ekman flow against the surface pressure gradient as:

$$\boldsymbol{\tau} \cdot \mathbf{u}_g^{(0)} = \rho_0 g \mathbf{U}_{\text{EK}} \cdot \nabla_h \bar{\eta}, \quad (\text{A1})$$

where $\mathbf{u}_g^{(0)}$ is the surface geostrophic current, \mathbf{U}_{EK} is the Ekman transport and η is the sea surface elevation (Roquet et al. 2011). This can be interpreted as the conversion of MKE into MAPE in the surface layer. We thus decompose $C(K_M, P_M)$ into the work done by Ekman flow and the work done by the ageostrophic current in the ocean interior:

$$C(K_M, P_M) = C^{(E)}(K_M, P_M) + C^{(I)}(K_M, P_M), \quad (\text{A2})$$

where

$$C^{(E)}(K_M, P_M) = \iint \rho_0 g \mathbf{U}_{\text{EK}} \cdot \nabla_h \bar{\eta} \, dx dy, \quad (\text{A3})$$

and

$$C^{(I)}(K_M, P_M) = C(K_M, P_M) - C^{(E)}(K_M, P_M). \quad (\text{A4})$$

Figures A1(a)-(c) indicate that the spacing of the sea surface height contours becomes wider as the drag coefficient decreases. Since $C^{(E)}(K_M, P_M)$ is determined by the meridional sea surface height gradient in our case, the MAPE gain decreases with decreasing drag coefficient. Indeed, areas of prominent positive $C^{(E)}(K_M, P_M)$ in HIGH are wider than those of MEDIUM and LOW cases. Although the values near the standing meander are enhanced in the MEDIUM and HIGH cases compared with the LOW case, as shown later, this enhancement is not large enough to change the ranking of the domain-integrated values.

The horizontal distribution of $C^{(I)}(K_M, P_M)$ (Figures A1(d)-(f)) also highlights a key difference caused by the drag coefficient. In LOW and MEDIUM, negative values of $C^{(I)}(K_M, P_M)$ are evident along the southward western boundary current, while the magnitudes of $C^{(I)}(K_M, P_M)$ are much smaller in HIGH. When friction is weak, the flow becomes more barotropic (Figure 3) and the influence of bottom topography becomes pronounced (Figure 2). In MEDIUM and LOW, this results in the formation of a strong western boundary current. The pressure difference associated with the western boundary current accelerates its ageostrophic

component, which corresponds to the conversion of the MAPE into the MKE. It should be noted that the magnitudes of both the positive and negative values increase as drag coefficient decreases. However, the integrated value is always negative, and its magnitude increases with decreasing drag coefficient as seen below. The emergence of patchy positive and negative structures may be related to the phase of standing meanders.

Figure A2 summarizes the dependency of $C^{(E)}(K_M, P_M)$ and $C^{(I)}(K_M, P_M)$ on the drag. The Ekman work gradually increases with the drag coefficient. The value is smaller than 60 GW in the low-drag regime, and increases to more than 80 GW at $r = 10^{-2} \text{ m s}^{-1}$. Figure A2(b) shows that in the low-drag regime, $C^{(I)}(K_M, P_M)$ is approximately -15 GW , but its magnitude rapidly decreases above $r = 10^{-4} \text{ m s}^{-1}$, reflecting a reduction in the barotropic mode fraction (Figure 3) and associated weakening of the western boundary current. In summary, a decrease in the drag coefficient reduces the efficiency of APE gain by Ekman flow due to reduced surface geostrophic current. Additionally, the pressure gradient associated with the western boundary current promotes conversion from MAPE to MKE, further reducing $C(K_M, P_M)$.

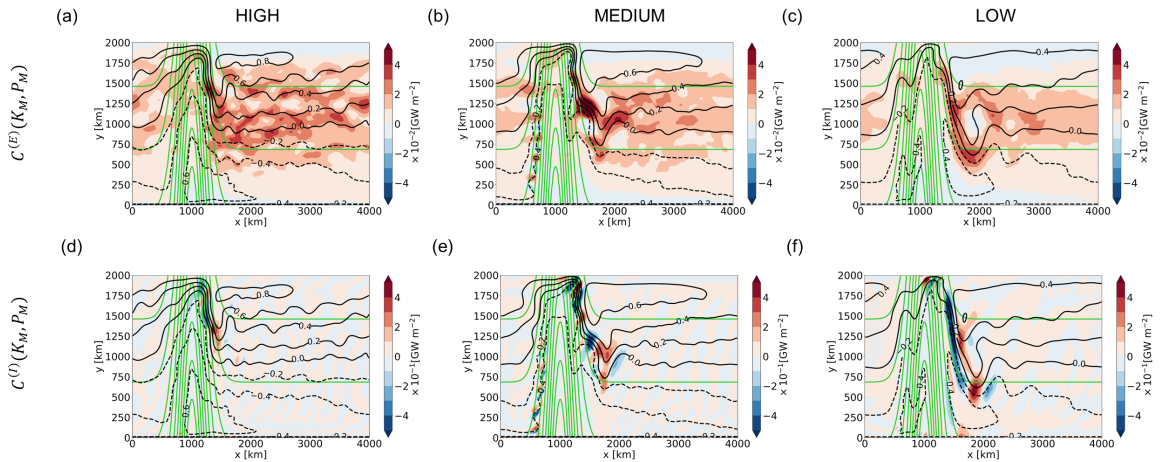


Figure A1. Horizontal distributions of $C^{(E)}(K_M, P_M)$ for (a) MEDIUM, (b) HIGH, and (c) LOW. Green contours are the same as those in Figure 2. Black contours are sea surface elevation contours with a contour interval of 0.2 m. Lower panel is same as the upper panel but for $C^{(I)}(K_M, P_M)$. Note that the color scale differs from that of the upper panel.

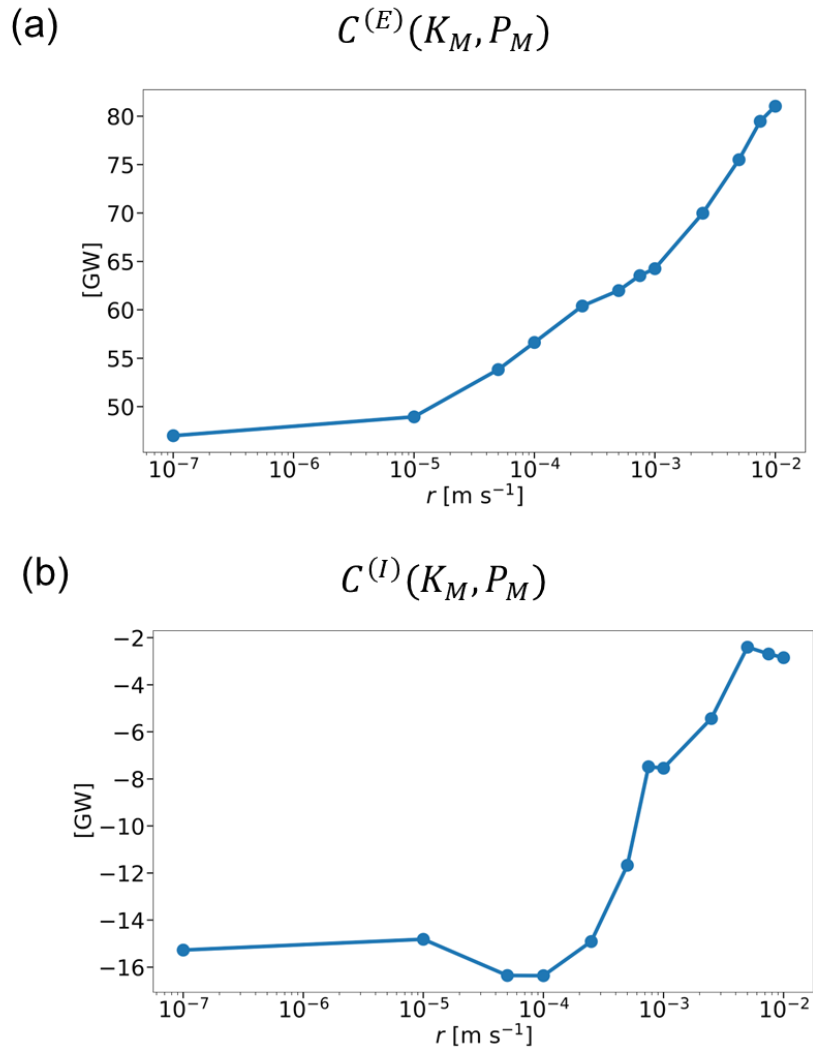


Figure A2 Curves of (a) $C^{(E)}(K_M, P_M)$ and (b) $C^{(I)}(K_M, P_M)$ as functions of drag coefficients.

Reference

- Abernathey, R., and P. Cessi, 2014: Topographic enhancement of Eddy efficiency in baroclinic equilibration. *J. Phys. Oceanogr.*, **44**, 2107–2126, <https://doi.org/10.1175/JPO-D-14-0014.1>.
- Aiki, H., and K. J. Richards, 2008: Energetics of the global ocean: The role of layer-thickness form drag. *J. Phys. Oceanogr.*, **38**, 1845–1869, <https://doi.org/10.1175/2008JPO3820.1>.
- , ———, and H. Sakuma, 2011: Maintenance of the mean kinetic energy in the global ocean by the barotropic and baroclinic energy routes: The roles of JEBAR and Ekman dynamics. *Ocean Dyn.*, **61**, 675–700, <https://doi.org/10.1007/s10236-011-0382-y>.
- Bischoff, T., and A. F. Thompson, 2014: Configuration of a Southern Ocean storm track. *J. Phys. Oceanogr.*, **44**, 3072–3078, <https://doi.org/10.1175/JPO-D-14-0062.1>.
- Chen, R., G. R. Flierl, and C. Wunsch, 2014: A description of local and nonlocal eddy-mean flow interaction in a global eddy-permitting state estimate. *J. Phys. Oceanogr.*, **44**, 2336–2352, <https://doi.org/10.1175/JPO-D-14-0009.1>.
- Constantinou, N. C., 2018: A barotropic model of eddy saturation. *J. Phys. Oceanogr.*, **48**, 397–411, <https://doi.org/10.1175/JPO-D-17-0182.1>.
- , and W. R. Young, 2017: Beta-plane turbulence above monoscale topography. *J. Fluid Mech.*, **827**, 415–447, <https://doi.org/10.1017/jfm.2017.482>.
- , and A. M. C. Hogg, 2019: Eddy Saturation of the Southern Ocean: A Baroclinic Versus Barotropic Perspective. *Geophys. Res. Lett.*, **46**, 12202–12212, <https://doi.org/10.1029/2019GL084117>.
- Danielson, R. E., J. R. Gyakum, and D. N. Straub, 2006: A case study of downstream baroclinic development over the North Pacific Ocean. Part I: Dynamical impacts. *Mon. Weather Rev.*, **134**, 1534–1548, <https://doi.org/10.1175/MWR3172.1>.
- Eaves, R. E., J. R. Maddison, D. P. Marshall, and S. Waterman, 2025: An Energy-and Enstrophy-Constrained Parameterization of Barotropic Eddy Potential Vorticity

- Fluxes. *J. Phys. Oceanogr.*, **55**, 573–591, <https://doi.org/10.1175/JPO-D-24-0027.1>.
- Hibiya, T., 2021: A new parameterization of turbulent mixing enhanced over rough seafloor topography. *Geophys. Res. Lett.*, 1–9, <https://doi.org/10.1029/2021gl096067>.
- Hogg, A. M. C., and J. R. Blundell, 2006: Interdecadal variability of the Southern Ocean. *J. Phys. Oceanogr.*, **36**, 1626–1645, <https://doi.org/10.1175/JPO2934.1>.
- James, I. N., and L. J. Gray, 1986: Concerning the effect of surface drag on the circulation of a baroclinic planetary atmosphere. *Quarterly Journal of the Royal Meteorological Society*, **112**, 1231–1250, <https://doi.org/10.1002/qj.49711247417>.
- Johnson, G. C., and H. L. Bryden, 1989: On the size of the Antarctic Circumpolar Current. *Deep Sea Research Part A. Oceanographic Research Papers*, **36**, 39–53, [https://doi.org/10.1016/0198-0149\(89\)90017-4](https://doi.org/10.1016/0198-0149(89)90017-4).
- Jouanno, J., and X. Capet, 2020: Connecting flow-topography interactions, vorticity balance, baroclinic instability and transport in the Southern Ocean: The case of an idealized storm track. *Ocean Science*, **16**, 1207–1223, <https://doi.org/10.5194/os-16-1207-2020>.
- Katsumata, K., 2017: Eddies observed by Argo floats. Part II: Form stress and streamline length in the Southern Ocean. *J. Phys. Oceanogr.*, **47**, 2237–2250, <https://doi.org/10.1175/JPO-D-17-0072.1>.
- Klymak, J. M., 2018: Nonpropagating form drag and turbulence due to stratified flow over large-scale Abyssal Hill Topography. *J. Phys. Oceanogr.*, **48**, 2383–2395, <https://doi.org/10.1175/JPO-D-17-0225.1>.
- , D. Balwada, A. N. Garabato, and R. Abernathy, 2021: Parameterizing nonpropagating form drag over rough bathymetry. *J. Phys. Oceanogr.*, **51**, 1489–1501, <https://doi.org/10.1175/JPO-D-20-0112.1>.
- LaCasce, J. H., 2017: The Prevalence of Oceanic Surface Modes. *Geophys. Res. Lett.*, **44**, 11,097–11,105, <https://doi.org/10.1002/2017GL075430>.

- Large, W. G., J. C. McWilliams, and S. C. Doney, 1994: Oceanic vertical mixing: A review and a model with a nonlocal boundary layer parameterization. *Reviews of Geophysics*, **32**, 363–403, <https://doi.org/10.1029/94RG01872>.
- Lorenz, E. N., 1955: Available Potential Energy and the Maintenance of the General Circulation. *Tellus*, **7**, 157–167, <https://doi.org/10.1111/j.2153-3490.1955.tb01148.x>.
- Maddison, J. R., D. P. Marshall, J. Mak, and K. Maurer-Song, 2025: A Two-Dimensional Model for Eddy Saturation and Frictional Control in the Southern Ocean. *J. Adv. Model. Earth Syst.*, **17**, 2680–2684, <https://doi.org/10.1029/2024MS004682>.
- Mak, J., D. P. Marshall, J. R. Maddison, and S. D. Bachman, 2017: Emergent eddy saturation from an energy constrained eddy parameterisation. *Ocean Model. (Oxf)*, **112**, 125–138, <https://doi.org/10.1016/j.ocemod.2017.02.007>.
- , J. R. Maddison, D. P. Marshall, and D. R. Munday, 2018: Implementation of a geometrically informed and energetically constrained mesoscale eddy parameterization in an ocean circulation model. *J. Phys. Oceanogr.*, **48**, 2363–2382, <https://doi.org/10.1175/JPO-D-18-0017.1>.
- , A. Avdis, T. David, H. S. Lee, Y. Na, Y. Wang, and F. E. Yan, 2022a: On Constraining the Mesoscale Eddy Energy Dissipation Time-Scale. *J. Adv. Model. Earth Syst.*, **14**, <https://doi.org/10.1029/2022MS003223>.
- , D. P. Marshall, G. Madec, and J. R. Maddison, 2022b: Acute Sensitivity of Global Ocean Circulation and Heat Content to Eddy Energy Dissipation Timescale. *Geophys. Res. Lett.*, **49**, <https://doi.org/10.1029/2021GL097259>.
- Marshall, D. P., J. R. Maddison, and P. S. Berloff, 2012: A framework for parameterizing eddy potential vorticity fluxes. *J. Phys. Oceanogr.*, **42**, 539–557, <https://doi.org/10.1175/JPO-D-11-048.1>.
- , M. H. P. Ambaum, J. R. Maddison, D. R. Munday, and L. Novak, 2017: Eddy saturation and frictional control of the Antarctic Circumpolar Current. *Geophys. Res. Lett.*, **44**, 286–292, <https://doi.org/10.1002/2016GL071702>.

- Marshall, J., and G. Shutts, 1981: A Note on Rotational and Divergent Eddy Fluxes. *J. Phys. Oceanogr.*, **11**, 1677–1680, [https://doi.org/10.1175/1520-0485\(1981\)011<1677:ANORAD>2.0.CO;2](https://doi.org/10.1175/1520-0485(1981)011<1677:ANORAD>2.0.CO;2).
- , and T. Radko, 2003: Residual-Mean Solutions for the Antarctic Circumpolar Current and Its Associated Overturning Circulation. *J. Phys. Oceanogr.*, **33**, 2341–2354, [https://doi.org/10.1175/1520-0485\(2003\)033<2341:RSFTAC>2.0.CO;2](https://doi.org/10.1175/1520-0485(2003)033<2341:RSFTAC>2.0.CO;2).
- , A. Adcroft, C. Hill, L. Perelman, and C. Heisey, 1997: A finite-volume, incompressible Navier Stokes model for studies of the ocean on parallel computers. *J. Geophys. Res. Oceans*, **102**, 5753–5766, <https://doi.org/10.1029/96JC02775>.
- Matsuta, T., and Y. Masumoto, 2021: Modified View of Energy Budget Diagram and Its Application to the Kuroshio Extension Region. *J. Phys. Oceanogr.*, **51**, 1163–1175, <https://doi.org/10.1175/JPO-D-20-0124.1>.
- , and ———, 2023: Energetics of the Antarctic Circumpolar Current. Part I: The Lorenz Energy Cycle and the Vertical Energy Redistribution. *J. Phys. Oceanogr.*, **53**, 1467–1484, <https://doi.org/10.1175/jpo-d-22-0133.1>.
- , and H. Mitsudera, 2024: Inertial Effect and Its Dependency on the Topographic Geometries in Barotropic Channel Models under the Weakly Nonlinear Regime. *J. Phys. Oceanogr.*, **54**, 1267–1283, <https://doi.org/10.1175/jpo-d-23-0075.1>.
- , ———, Y. Masumoto, H. Sasaki, R. Furue, and T. Ogata, 2024: Enhanced eddy activity along the Subantarctic Front under intensified westerly winds. *Ocean Dyn.*, <https://doi.org/10.1007/s10236-024-01644-5>.
- Munday, D. R., H. L. Johnson, and D. P. Marshall, 2015: The role of ocean gateways in the dynamics and sensitivity to wind stress of the early Antarctic Circumpolar Current. *Paleoceanography*, **30**, 284–302, <https://doi.org/10.1002/2014PA002675>.
- Murakami, S., 2011: Atmospheric local energetics and energy interactions between mean and eddy fields. Part I: Theory. *J. Atmos. Sci.*, **68**, 760–768, <https://doi.org/10.1175/2010JAS3664.1>.
- Nadeau, L. P., and D. N. Straub, 2012: Influence of wind stress, wind stress curl, and bottom friction on the transport of a model antarctic circumpolar current. *J. Phys. Oceanogr.*, **42**, 207–222, <https://doi.org/10.1175/JPO-D-11-058.1>.

- , and R. Ferrari, 2015: The role of closed gyres in setting the zonal transport of the antarctic circumpolar current. *J. Phys. Oceanogr.*, **45**, 1491–1509, <https://doi.org/10.1175/JPO-D-14-0173.1>.
- Naveira Garabato, A. C., A. J. George Nurser, R. B. Scott, and J. A. Goff, 2013: The impact of small-scale topography on the dynamical balance of the ocean. *J. Phys. Oceanogr.*, **43**, 647–668, <https://doi.org/10.1175/JPO-D-12-056.1>.
- , K. L. Polzin, R. Ferrari, J. D. Zika, and A. Forryan, 2016: A microscale view of mixing and overturning across the Antarctic Circumpolar Current. *J. Phys. Oceanogr.*, **46**, 233–254, <https://doi.org/10.1175/JPO-D-15-0025.1>.
- Olbers, D., J. Willebrand, and C. Eden, 2012: *Ocean Dynamics*. Springer Berlin Heidelberg, <https://doi.org/10.1007/978-3-642-23450-7>.
- Pedlosky, J., 1987: *Geophysical Fluid Dynamics*. Springer New York, <https://doi.org/10.1007/978-1-4612-4650-3>.
- Phillips, H. E., and S. R. Rintoul, 2000: Eddy variability and energetics from direct current measurements in the Antarctic Circumpolar Current south of Australia. *J. Phys. Oceanogr.*, **30**, 3050–3076, [https://doi.org/10.1175/1520-0485\(2000\)030<3050:EVAEFD>2.0.CO;2](https://doi.org/10.1175/1520-0485(2000)030<3050:EVAEFD>2.0.CO;2).
- Rivière, P., A. M. Treguier, and P. Klein, 2004: Effects of Bottom Friction on Nonlinear Equilibration of an Oceanic Baroclinic Jet. *J. Phys. Oceanogr.*, **34**, 416–432, [https://doi.org/10.1175/1520-0485\(2004\)034<0416:EOBFON>2.0.CO;2](https://doi.org/10.1175/1520-0485(2004)034<0416:EOBFON>2.0.CO;2).
- Roquet, F., C. Wunsch, and G. Madec, 2011: On the patterns of wind-power input to the ocean circulation. *J. Phys. Oceanogr.*, **41**, 2328–2342, <https://doi.org/10.1175/JPO-D-11-024.1>.
- Solodoch, A., A. L. Stewart, and J. C. McWilliams, 2016: Baroclinic instability of axially symmetric flow over sloping bathymetry. *J. Fluid Mech.*, **799**, 265–296, <https://doi.org/10.1017/jfm.2016.376>.
- Stewart, A. L., N. K. Neumann, and A. Solodoch, 2023: “Eddy” Saturation of the Antarctic Circumpolar Current by Standing Waves. *J. Phys. Oceanogr.*, **53**, 1161–1181, <https://doi.org/10.1175/jpo-d-22-0154.1>.

- Von Storch, J. S., C. Eden, I. Fast, H. Haak, D. Hernández-Deckers, E. Maier-Reimer, J. Marotzke, and D. Stammer, 2012: An estimate of the Lorenz energy cycle for the World Ocean based on the 1/10°STORM/NCEP simulation. *J. Phys. Oceanogr.*, **42**, 2185–2205, <https://doi.org/10.1175/JPO-D-12-079.1>.
- Takahashi, A., and T. Hibiya, 2021: Influence of the Distortion of Vertical Wavenumber Spectra on Estimates of Turbulent Dissipation Using the Finescale Parameterization: Observations in the Antarctic Circumpolar Current. *J. Geophys. Res. Oceans*, **126**, <https://doi.org/10.1029/2020JC016613>.
- Takaya, K., and H. Nakamura, 2001: A formulation of a phase-independent wave-activity flux for stationary and migratory quasigeostrophic eddies on a zonally varying basic flow. *J. Atmos. Sci.*, **58**, 608–627, [https://doi.org/10.1175/1520-0469\(2001\)058<0608:AFOAPI>2.0.CO;2](https://doi.org/10.1175/1520-0469(2001)058<0608:AFOAPI>2.0.CO;2).
- Thompson, A. F., and A. C. Naveira Garabato, 2014: Equilibration of the Antarctic Circumpolar Current by standing meanders. *J. Phys. Oceanogr.*, **44**, 1811–1828, <https://doi.org/10.1175/JPO-D-13-0163.1>.
- Torres, R., R. Waldman, G. Madec, C. de Lavergne, R. Séférian, and J. Mak, 2025: An Energetically and Observationally Constrained Mesoscale Parameterization for Ocean Climate Models. *J. Adv. Model. Earth Syst.*, **17**, <https://doi.org/10.1029/2025MS005394>.
- Trossman, D. S., B. K. Arbic, J. G. Richman, S. T. Garner, S. R. Jayne, and A. J. Wallcraft, 2016: Impact of topographic internal lee wave drag on an eddying global ocean model. *Ocean Model. (Oxf.)*, **97**, 109–128, <https://doi.org/10.1016/j.ocemod.2015.10.013>.
- Wang, L., and R. X. Huang, 1995: A Linear Homogeneous Model of Wind-Driven Circulation in a β -Plane Channel. *J. Phys. Oceanogr.*, **25**, 587–603, [https://doi.org/10.1175/1520-0485\(1995\)025<0587:ALHMOW>2.0.CO;2](https://doi.org/10.1175/1520-0485(1995)025<0587:ALHMOW>2.0.CO;2).
- Ward, M. L., and A. M. C. Hogg, 2011: Establishment of momentum balance by form stress in a wind-driven channel. *Ocean Model. (Oxf.)*, **40**, 133–146, <https://doi.org/10.1016/j.ocemod.2011.08.004>.

- Waterman, S., A. C. Naveira Garabato, and K. L. Polzin, 2013: Internal waves and turbulence in the antarctic circumpolar current. *J. Phys. Oceanogr.*, **43**, 259–282, <https://doi.org/10.1175/JPO-D-11-0194.1>.
- Wu, Y., Z. Wang, and C. Liu, 2017: On the response of the Lorenz energy cycle for the Southern Ocean to intensified westerlies. *J. Geophys. Res. Oceans*, **122**, 2465–2493, <https://doi.org/10.1002/2016JC012539>.
- Yang, L., M. Nikurashin, A. M. Hogg, and B. M. Sloyan, 2018: Energy loss from transient eddies due to lee wave generation in the Southern Ocean. *J. Phys. Oceanogr.*, **48**, 2867–2885, <https://doi.org/10.1175/JPO-D-18-0077.1>.
- , ——, A. M. Hogg, and B. M. Sloyan, 2023: Lee Waves Break Eddy Saturation of the Antarctic Circumpolar Current. *Geophys. Res. Lett.*, **50**, <https://doi.org/10.1029/2023GL103866>.
- Youngs, M. K., A. F. Thompson, A. Lazar, and K. J. Richards, 2017: ACC meanders, energy transfer, and mixed barotropic-baroclinic instability. *J. Phys. Oceanogr.*, **47**, 1291–1305, <https://doi.org/10.1175/JPO-D-16-0160.1>.
- Zemskova, V. E., B. L. White, and A. Scotti, 2015: Available potential energy and the general circulation: Partitioning wind, buoyancy forcing, and diapycnal mixing. *J. Phys. Oceanogr.*, **45**, 1510–1531, <https://doi.org/10.1175/JPO-D-14-0043.1>.
- Zhang, X., M. Nikurashin, B. Peña-Molino, S. R. Rintoul, and E. Doddridge, 2024: Maintenance of the Zonal Momentum Balance of the Antarctic Circumpolar Current by Barotropic Dynamics. *J. Phys. Oceanogr.*, **54**, 1565–1581, <https://doi.org/10.1175/jpo-d-23-0042.1>.
- Zhu, H. Y., T. Y. Pei, J. H. Xie, and K. Q. Xia, 2025: Zonal jets over small-scale topography: Jet properties and energy transfers. *J. Fluid Mech.*, **1020**, <https://doi.org/10.1017/jfm.2025.10566>.